Supporting Information for

Porous organic polymer for symmetric sodium dual-ion battery through adsorption-intercalation-insertion mechanism

Suprabhat Sarkar,[a] Tapas Kumar Dutta,[a] Balaji Prasad Mandal,[b] Abhijit Patra[*a]*

[a]Department of Chemistry, Indian Institute of Science Education and Research Bhopal, Bhopal 462066, Madhya Pradesh, India
Fax: +91 (0)755 409 2392; Tel: +91 (0)755 669 1337
Email: abhijit@iiserb.ac.in

[b]Chemistry Division, Bhabha Atomic Research Centre, Mumbai-400 085, India

Contents

I. Instrumentation and methods

Nuclear magnetic resonance (NMR) spectroscopy: Bruker Avance III 500 MHz NMR spectrometer

Attenuated total reflectance Fourier transform infrared (ATR FTIR) spectroscopy: Perkin-Elmer Model UATR Spectrum Two instrument in the range of 4000 to 500 cm^{-1}

Raman spectroscopic analysis: LabRAM HR Raman spectrometer (HORIBA) with a 632 nm laser excitation and a 50x long working distance objective

Powder X-ray diffraction (PXRD): PANalytical Empyrean XRD instrument using Cu Kα1 radiation source at a wavelength of 1.5405 Å

Thermogravimetric analysis (TGA): Perkin Elmer TGA-6000 instrument

XPS analysis: PHI 5000 Versa Prob II, FIE Inc instrument

Elemental analysis (CHNS analysis): Elementar Vario Micro Cube

Field emission scanning electron microscopy (FESEM): Carl Zeiss Ultraplus electron microscope

High-resolution transmission electron microscopy (HRTEM): FEI TALOS 200S transmission electron microscope (accelerating voltage of 200 kV); the samples were prepared by drop-casting onto a lacey carbon-coated 400 mesh Cu grid.

Brunauer–Emmett–Teller (BET) specific surface area measurements: Quantachrome Autosorb iQ-XR instruments; BET surface area and pore width were calculated using ASiQwin software

Electrochemical measurements: BioLogic SP-300 potentiostat (BioLogic, France)
Coin-cell battery testing: Neware battery tester (BTS-5V50mA, model: CT-4008)

II. Synthesis

A. Chemicals:

1,3,6,8-Tetrabromopyrene, bis(dibenzylideneacetone)palladium(0) [$Pd(dba)_2$], 2-dicyclohexylphosphino-2′,4′,6′-triisopropylbiphenyl (XPhos), anhydrous toluene (99.8%), sodium hexafluorophosphate ($NaPF_6$), carboxymethyl cellulose (CMC), diethylene glycol dimethyl ether (diglyme) were procured from Sigma Aldrich. Tris(4-aminophenyl)amine was obtained from BLD Pharma, India. Potassium tertiarybutoxide (^tBuOK) and sodium metal were purchased from Spectrochem. Acetylene black was obtained from Alfa Aesar, India. Methanol and chloroform were procured from Finar Chemicals. 2032 type coin cell components, battery grade copper, and aluminum foils were obtained from MatLab Technologies, India.

B. Synthesis of TPA-Py porous organic polymer:

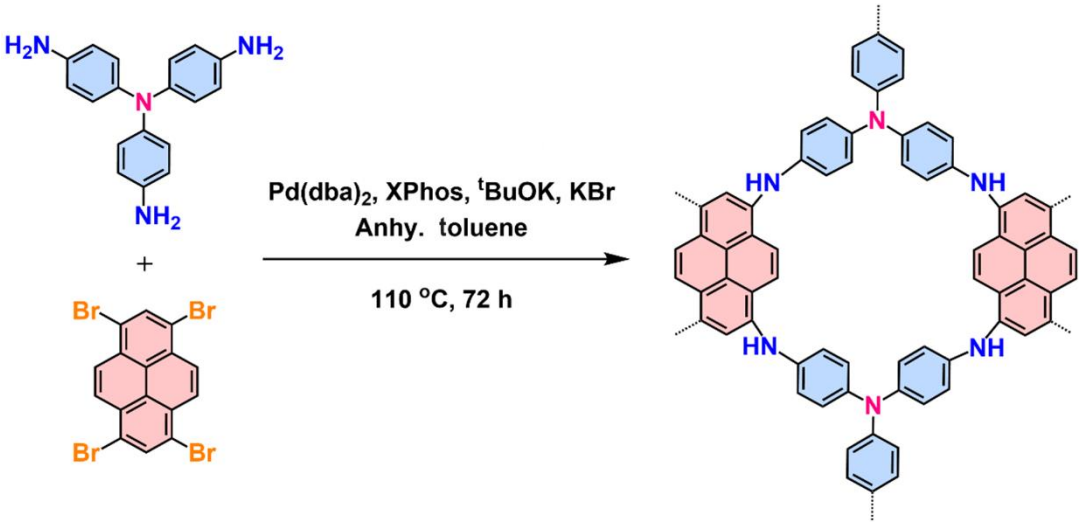

Scheme S1: Schematic illustration of pyrene-based conjugated porous organic polymers (TPA-Py) synthesis by a Buchwald-Hartwig (BH) coupling reaction.

The TPA-Py porous organic polymer (POP) was fabricated through the palladium-catalyzed Buchwald-Hartwig coupling reaction between tris(4-aminophenyl)amine and 1,3,6,8-tetrabromopyrene as per the previous protocol.[S1,S2] Briefly, tris(4-aminophenyl)amine, 1,3,6,8-tetrabromopyrene, and ^{t}BuOK, were charged in a 100 mL Schlenk tube and sealed using a rubber septum. The catalyst $Pd(dba)_2$ and phosphine ligand (XPhos) were added under an inert atmosphere. 20 mL anhydrous toluene was added to it, and the whole mixture was subjected to three consecutive freeze-pump-thaw cycles under a nitrogen atmosphere to remove any adsorbed gases. The sealed Schlenk tube was kept under stirring at 110 °C for 72 h. The reaction product was quenched with 5% HCl containing methanol, and the solid product was then filtered out. The solid was washed thoroughly with methanol and then subjected to Soxhlet extraction with methanol and chloroform each for 24 h. Then, the polymer was dried in a drying oven for 12 h at 65 °C and finally in a vacuum oven at 120 °C for 24 h prior to further characterization. The yield of TPA-Py POP is ~71%.

III. Characterizations

A. Nitrogen gas adsorption analysis:

TPA-Py POP was degassed for 12 h at 120 °C in a high vacuum before the gas adsorption analysis. The nitrogen adsorption-desorption analysis was conducted at 77 K. The specific surface area was calculated from the N_2 adsorption-desorption isotherm using the Brunauer-Emmett-Teller (BET) method. The linear BET region was selected from the Rouquerol plot, taking into account the linear progression of $V(1-P/P_0)$ with relative pressure (P/P_0) (Fig. S1a). The BET surface area plot was obtained using the following equation (Fig. S1b).[S3]

$$\frac{P/P_0}{n\left(1-\frac{P}{P_0}\right)} = \frac{1}{n_m C} + \frac{C-1}{n_m C}(P/P_0) \qquad \text{... S1}$$

Where, P/P_0 = relative pressure

n = amount of adsorbate at P/P_0

n_m = monolayer capacity

C = the BET constant

A relative pressure range of $0.05 < P/P_0 < 0.3$ was employed to ascertain the specific surface areas of TPA-Py POP. The pore size was estimated from the N_2 adsorption-desorption isotherm employing the non-local density functional theory (NLDFT) method (carbon, slit pore, equilibrium model, Fig. S2).

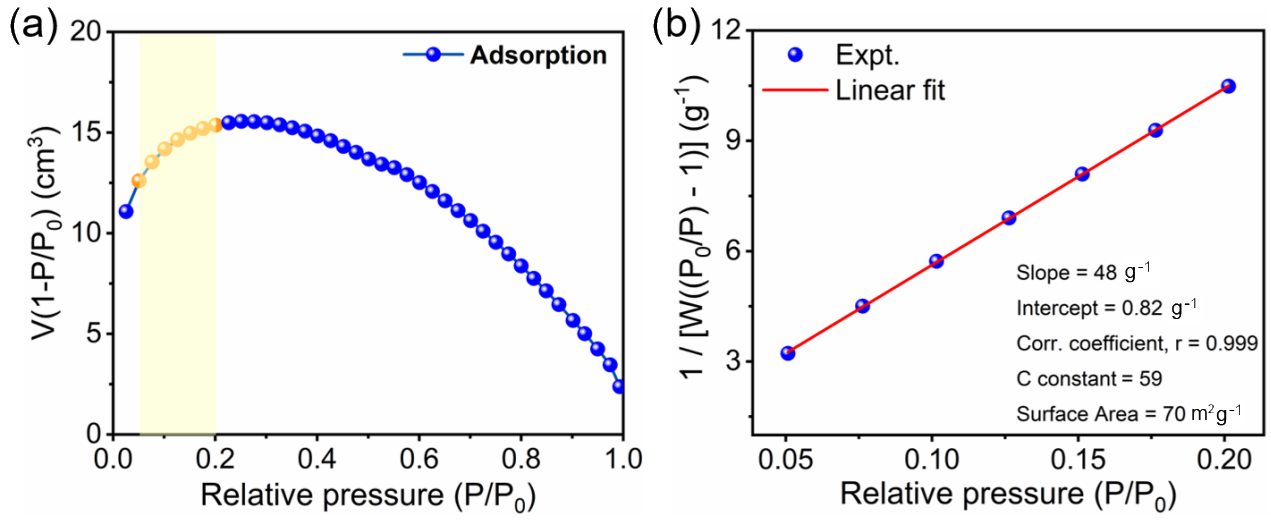

Fig. S1 (a) Rouquerol plot indicating the selected data points for linear BET equation. (b) Linear BET plot within the pressure range of $0.05 < P/P_0 < 0.3$ for the surface area calculation.

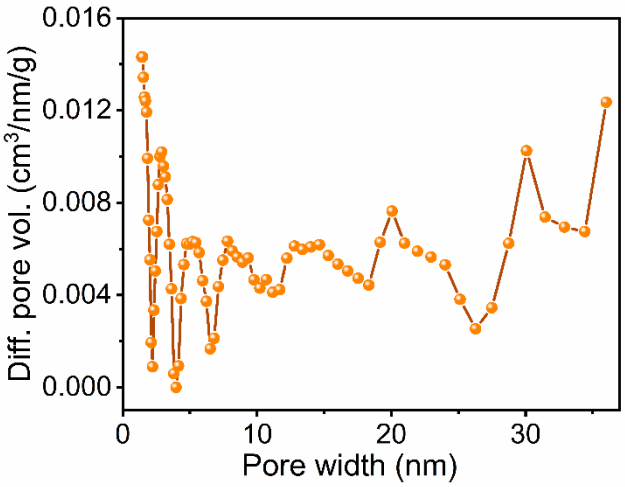

Fig. S2 Pore-size distribution of TPA-Py POP obtained from nitrogen adsorption-desorption isotherm using the non-local density functional theory method.

B. Powder X-ray diffraction (PXRD) analysis

The comparative PXRD pattern shows a broad peak for TPA-Py POP, indicating its amorphous character (Fig. S3). The crystalline peaks of the starting monomers are absent in the PXRD pattern of TPA-Py POP, suggesting no unreacted monomers trapped within the POP network. However, a small

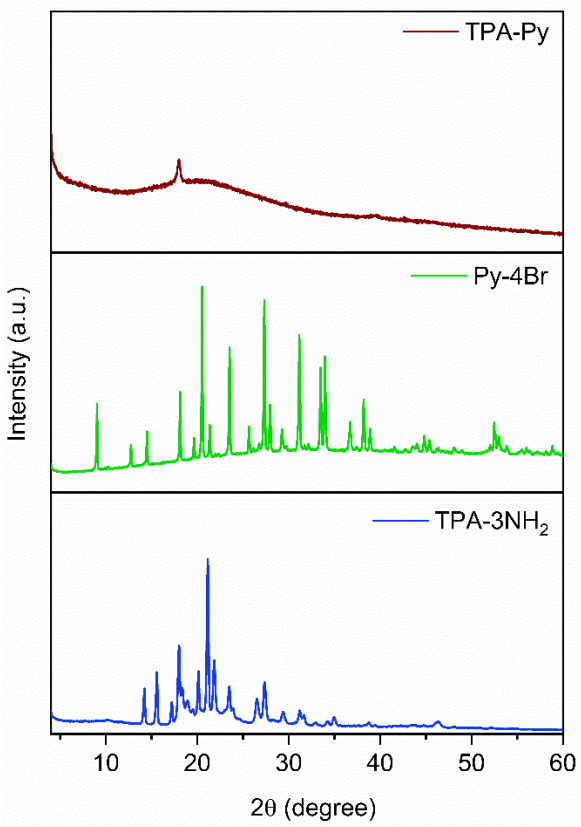

Fig. S3 Comparative powder X-ray diffraction (PXRD) profile of tris(4-aminophenyl)amine, 1,3,6,8-tetrabromopyrene and TPA-Py porous organic polymer.

sharp peak at 2θ ~18° may be due to some semicrystalline character induced by the π-π stacking of a few pyrene units within the polymer network (Fig. S3).[S4]

C. Elemental analysis

The elemental composition of TPA-Py POP was estimated by CHNS elemental analysis (**Table S1**). The experimental elemental composition of the polymer closely resembled the calculated composition. A probable repeating unit of TPA-Py was proposed based on the elemental analysis (Fig. S4).[S5,S6]

Table S1 Experimental and calculated CHNS elemental analysis data of TPA-Py POP.

POP	Probable chemical formula of repeating unit	C		H		N		Br[$]	O[#]
		Cal.	Expt.	Cal.	Expt.	Cal.	Expt.	Cal.	Cal.
TPA-Py	$C_{50}H_{32}BrN_6.3H_2O$	70.59	66.65	4.50	4.14	9.88	9.50	9.39	5.64

Note: [$]Bromine was found in the XPS analysis (*vide infra*). [#]The oxygen amount was attributed to the trapped moisture, as we found the characteristic peak in XPS analysis. The trapped water was found to be ~6 wt% calculated from the total molecular weight of the repeating unit.

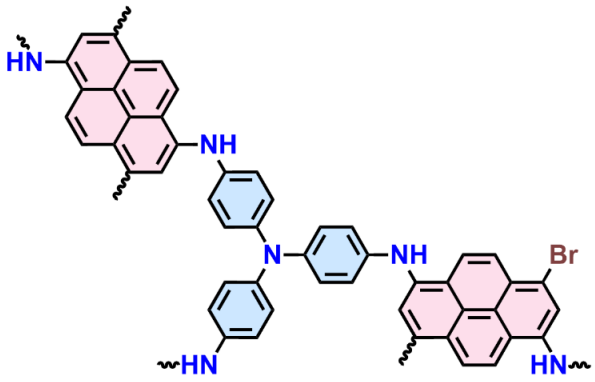

Fig. S4 Probable repeating unit of TPA-Py POP formulated from the elemental analysis.

D. X-ray photoelectron spectroscopy (XPS) analysis

The XPS analysis of the TPA-Py revealed the presence of C1s and N1s, respectively, at ~285 and 399 eV. The O1s peak could be due to the adsorbed moisture (Fig. S5). A very small peak of Br3d might originate from the terminal end groups of pyrene moieties (Fig. S5). The high-resolution N1s spectra show a single peak. The peaks for secondary and tertiary nitrogen atoms are very closely spaced and cannot be deconvoluted separately (Fig. S6). Similar observations have been reported earlier.[S2]

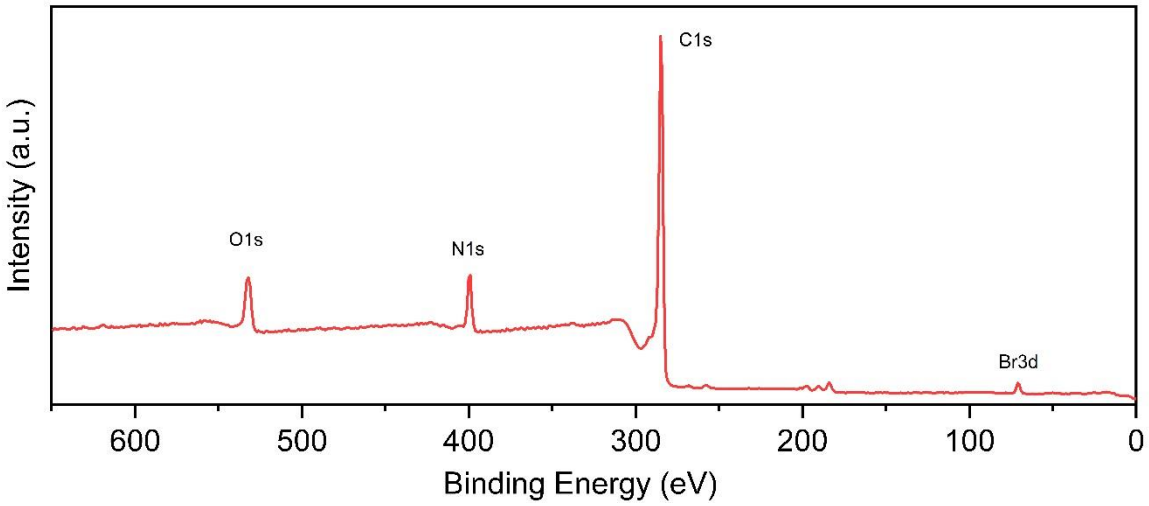

Fig. S5 Full scan XPS spectrum of TPA-Py porous organic polymer.

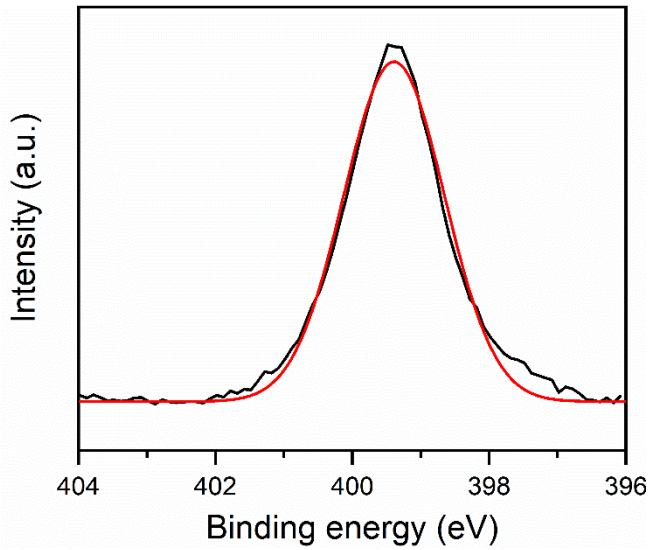

Fig. S6 High resolution N1s XPS spectra of TPA-Py porous organic polymer peaked at ~399 eV; black: raw data, red: fitted data.

IV. Electrochemical characterization and analysis

A. Electrochemical characterizations

All the electrochemical analyses were carried out by fabricating CR2032 coin cells. The electrode was fabricated using TPA-Py POP as the active material. A slurry was prepared by homogeneous mixing of TPA-Py POP (60%) with a conductive agent (acetylene black, 20%) and binder (carboxymethyl cellulose, 20%) in water. The slurry was coated separately on clean copper and aluminum foils for anode and cathode, respectively, and dried at 75 °C for 24 h. The dried copper and aluminum foils were pressed using a hydraulic hot-roll press at 80 °C. Then, these foils were cut into 14 mm circular discs using a disc-cutting machine (model: MT-CP60, MatLab India). The small disc-shaped electrodes were again dried and weighed to find out the amount of active material loading. For preparing sodium-ion half-cells, the circular disc electrodes were used against a clean sodium foil separated by a polypropylene separator. The cell was flooded with electrolytes containing 1 M sodium hexafluorophosphate ($NaPF_6$) dissolved in diethylene glycol dimethyl ether (diglyme) before sealing. As mentioned before, the symmetric full-cell organic battery was fabricated similarly using TPA-Py polymer coated on aluminum foils and 1 M $NaPF_6$ in diglyme as an electrolyte. All the cells were fabricated using an N_2-filled glove box with H_2O and O_2 content less than 0.5 ppm. The cells were allowed to equilibrate for 2 h before the electrochemical analysis. The electrochemical impedance spectroscopy (EIS) and cyclic voltammetry (CV) of the fabricated coin cells were tested using a Biologic SP300 electrochemical workstation. All the galvanostatic charge-discharge (GCD) experiments were carried out using the NEWARE battery testing system (BTS-5V50mA, model: CT-4008). The diffusion of sodium ion (Na^+) and hexafluorophosphate (PF_6^-) ions was measured using galvanostatic intermittent titration techniques (GITT) using the same electrochemical workstation.

B. Cyclic voltammetry

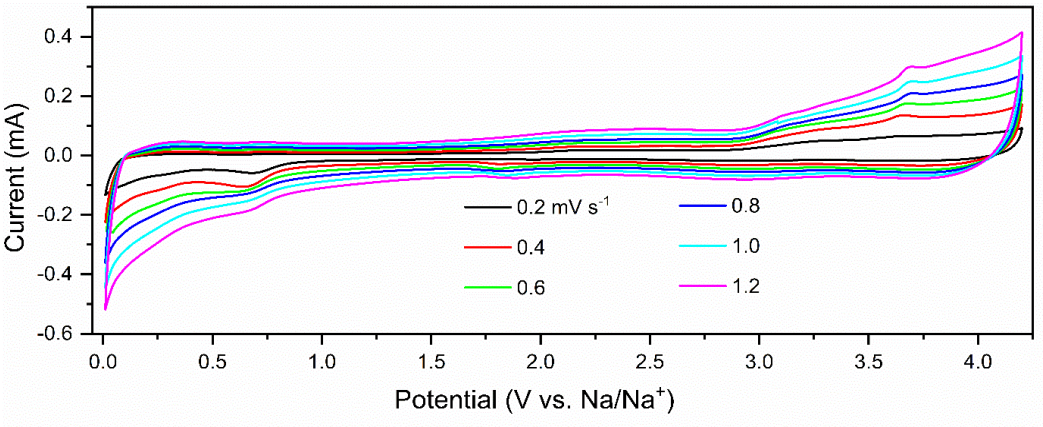

Fig. S7 Cyclic voltammogram of TPA-Py POP at 0.2, 0.4, 0.6, 0.8, 1.0, and 1.2 mV s^{-1} scan rate with a potential range of 0.01 to 4.2 V covering the whole potential window of cathodic and anodic reactions.

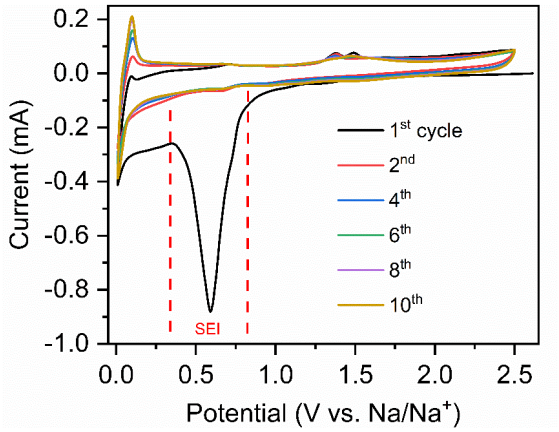

Fig. S8 Cyclic voltammograms of first 10 cycles at 0.2 mV s^{-1} scan rate for anodic reactions of TPA-Py polymer. The strong irreversible reduction peak between ~0.3 to 0.9 V at the first cycle represents the solid electrolyte interphase (SEI) formation.

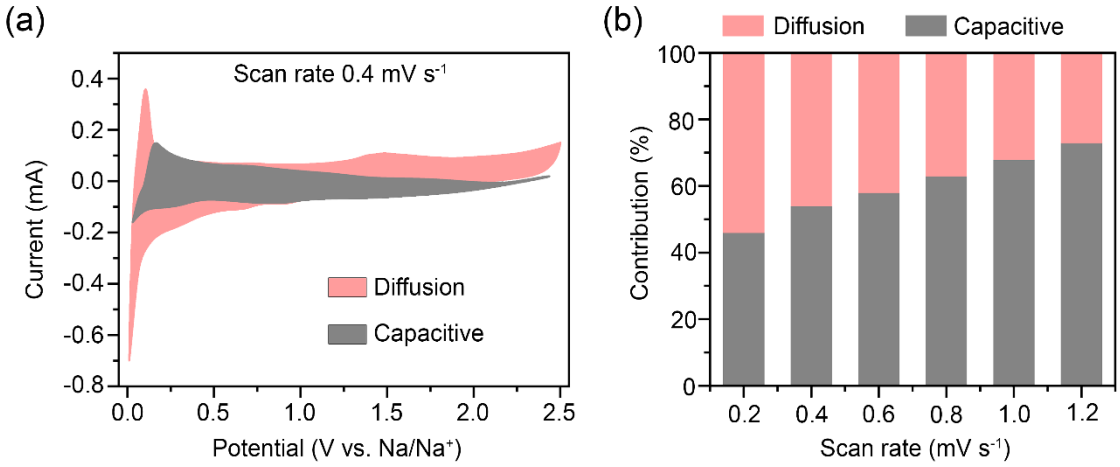

Fig. S9 (a) CV profile for TPA-Py POP when used as an anode at a scan rate of 0.4 mV s^{-1}. The estimated capacitive current contribution is shown in the 'grey' shaded region. (b) The capacitive and diffusion contribution of TPA-Py POP at different scan rates, 0.2, 0.4, 0.6, 0.8, 1.0, and 1.2 mV s^{-1}.

C. Galvanostatic charge-discharge (GCD) experiments:

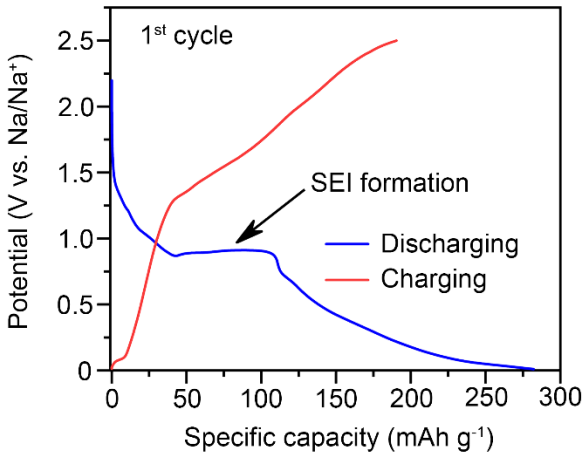

Fig. S10 First GCD profile of TPA-Py POP using half-cell at 20 mA g^{-1} current density.

The symmetric dual-ion batteries have been fabricated using TPA-Py polymer in both the cathode and the anode. The resulting GCD profiles of the full cell at 20 mA g^{-1} current density is shown in Fig. 3d, and the cyclic stability of the SDIB is shown in Fig. S10b, indicating the maximum specific capacity of ~21 mAh g^{-1}. The resulting low to moderate specific capacity of the full cell could be attributed to the inherent issue of low solubility of $NaPF_6$ in diglyme solvent (diethylene glycol dimethyl ether) to achieve higher molar concentration (beyond 1 M).[S7,S8] The electrolyte is the only source of Na^+ and PF_6^- ions for dual-ion batteries; hence, the low concentration of the electrolyte in the present case might be one of the limiting factors and paves the way for further investigations in the future.

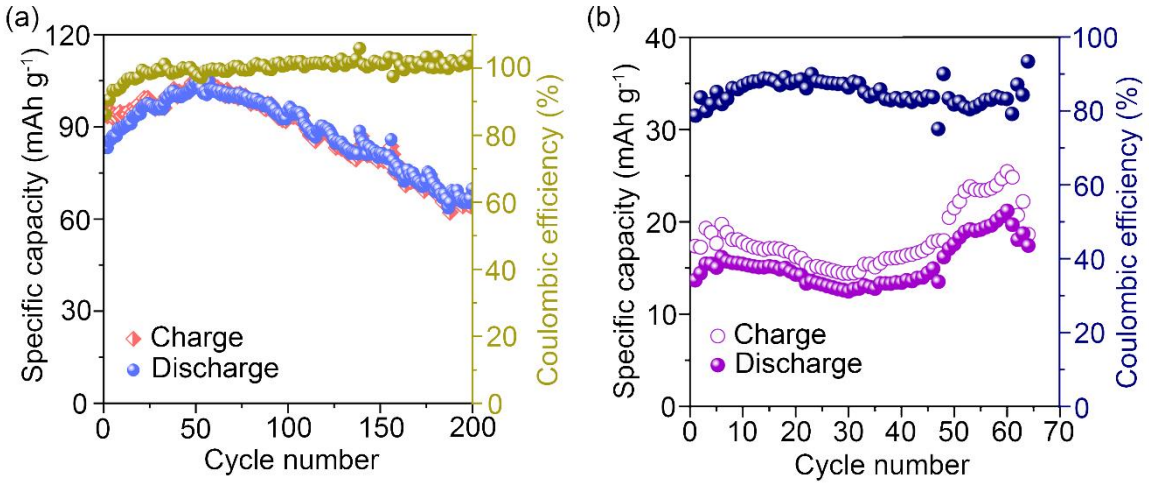

Fig. S11 (a) Cyclic stability of TPA-Py POP for 200 cycles using galvanostatic charge-discharge study at 20 mA g^{-1} current density. (b) Cyclic stability of TPA-Py POP based symmetric sodium-based dual-ion battery using galvanostatic charge-discharge study at 20 mA g^{-1} current density.

D. Calculation of diffusion coefficient using galvanostatic intermittent titration technique (GITT)

The diffusion coefficient of both cations (Na^+) and anion (PF_6^-) have been analyzed by using the galvanostatic intermittent titration technique (GITT) following the below equation.[S9]

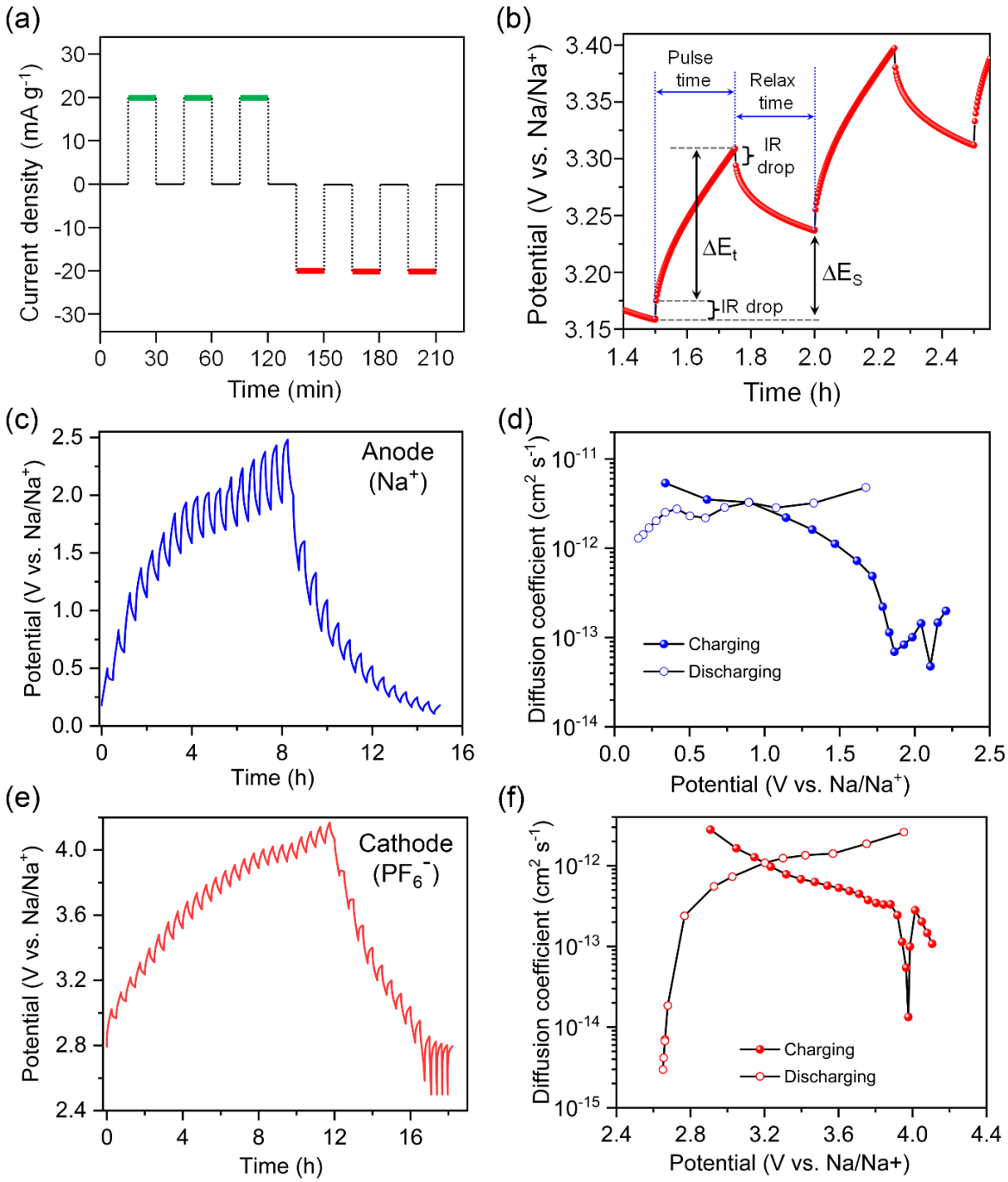

Fig. S12 (a) Galvanostatic intermittent titration technique (GITT) experimental conditions during charge-discharge for anodic and cathodic reactions. (b) Corresponding variations in potential during the 20 mA g^{-1} charging current pulses and relaxation period representing ΔE_t, ΔE_s, and IR drop. GITT curves of TPA-Py POP for (c) cation (Na^+) and (e) anion (PF_6^-) diffusion process. Diffusion coefficients at different potentials during (d) sodiation-desodiation and (f) PF_6^- insertion and deinsertion in TPA-Py POP.

$$D = \frac{4}{\pi\tau}\left(\frac{1}{S_{BET}} \times \frac{1}{\rho}\right)^2 \left(\frac{\Delta E_S}{\Delta E_t}\right)^2 \quad \ldots S2$$

Where,

τ = pulse time period = 15 min

S_{BET} = surface area of the porous materials

ρ = tap density of the electrode (can be measured from the mass and volume of the electrode = $\pi r^2 h$)

ΔE_s = change in the steady-state voltage

ΔE_t = voltage change in a single-step GITT experiment

E. Electrochemical impedance spectroscopy (EIS) analysis

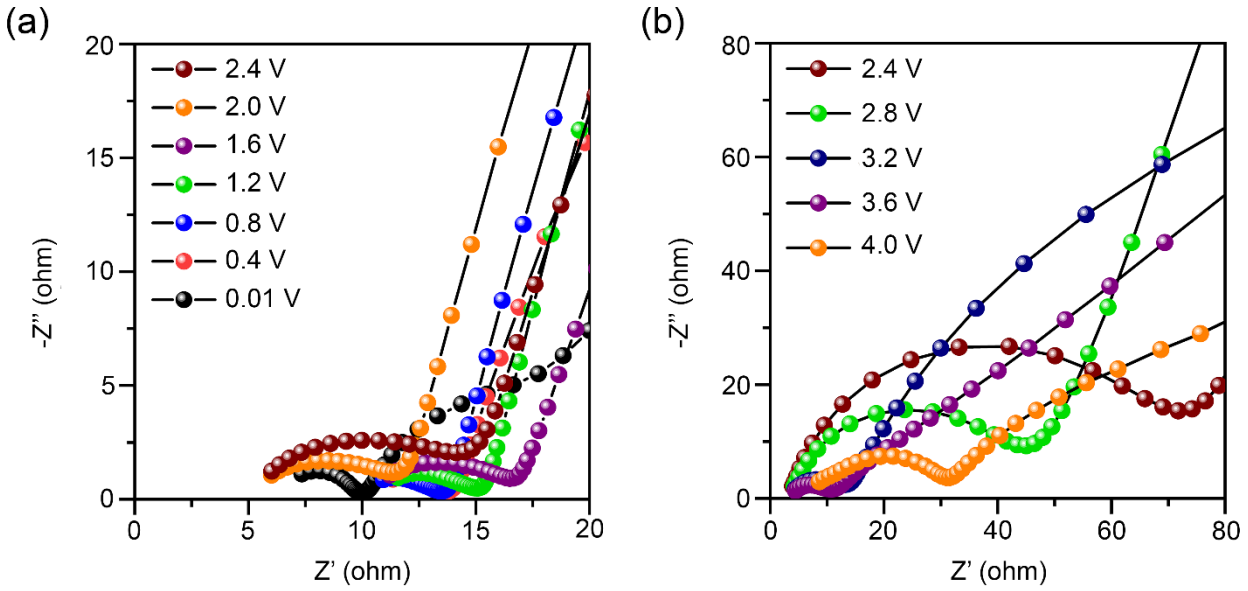

Fig. S13 Potentiostatic EIS spectra of TPA-Py POP at different potentials reflecting decreasing charge-transfer resistance (R_{CT}) with increasing potential bias as (a) anode and (b) cathode.

F. Batch-wise reproducibility of electrochemical data

Table S2 The specific capacities (C_{sp}, mAh g^{-1}) of TPA-Py porous organic polymer at various current densities from three independent measurements for the samples obtained from different synthesis batches.

Anodic [Na^+ ion storage]			
Current density (mA g^{-1})	**Specific capacity (mAh g^{-1})**		
	Batch 1	**Batch 2**	**Batch 3**
20	106	72	92
50	79	57	72
100	62	47	59
200	45	35	47
500	29	26	33
1000	22	18	24
2000	14	15	18
Cathodic [PF_6^- ion storage]			
Current density (mA g^{-1})	**Specific capacity (mAh g^{-1})**		
	Batch 1	**Batch 2**	**Batch 3**
20	65	64	55
50	48	45	47
100	36	35	37
200	28	27	28
500	17	17	20
1000	12	12	14
2000	07	06	08

G. Plausible mechanism of dual-ion storage

(i) Na^+ ion storage (Anodic):

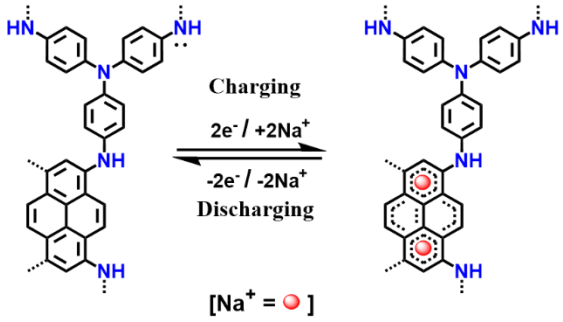

Cell	Negative electrode	Positive electrode
Electrolytic cell (charging) Electrical energy is used to drive reaction	Na-metal ⟶ $xNa^+ + xe^-$ Sodium is oxidized **Anode**	TPA-Py-POP + $xNa^+ + xe^-$ ⟶ [TPA-Py-POP($Na)_x$] POP is reduced **Cathode**
Galvanic cell (discharge) Electrical energy is generated	[TPA-Py-POP($Na)_x$] ⟶ TPA-Py-POP + $xNa^+ + xe^-$ POP is oxidized **Anode**	$xNa^+ + xe^-$ ⟶ Na-metal Sodium is reduced **Cathode**

Fig. S14 Schematic illustration of cation-storage (Na^+) in TPA-Py polymer using adsorption-intercalation mechanism during charging-discharging at anode.

(ii) PF_6^- ion storage (Cathodic):

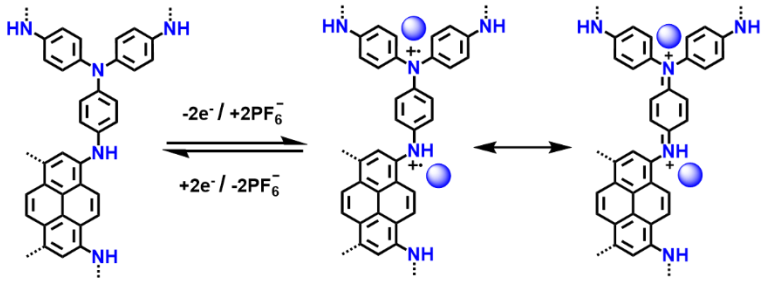

Cell	Negative electrode	Positive electrode
Electrolytic cell (charging) Electrical energy is used to drive reaction	[TPA-Py-POP] ⟶ ($Na^+ PF_6^-$) [TPA-Py-POP]$^{x+}$ [PF_6^-]$_x$ + $xNa^+ + xe^-$ POP is oxidized **Anode**	$xNa^+ + xe^-$ ⟶ ($Na^+ PF_6^-$) Na-metal Sodium is reduced **Cathode**
Galvanic cell (discharge) Electrical energy is generated	Na-metal ⟶ ($Na^+ PF_6^-$) $xNa^+ + xe^-$ Sodium is oxidized **Anode**	[TPA-Py-POP]$^{x+}$ [PF_6^-]$_x$ + xe^- ⟶ ($Na^+ PF_6^-$) [TPA-Py-POP] + x[PF_6^-] POP is reduced **Cathode**

Fig. S15 Schematic illustration of the two-stage anion (PF_6^-) storage in TPA-Py polymer, using insertion into quaternized amine centers during charging-discharging at the cathode. Tertiary radical cation is more stable than the secondary ones, leading to two step oxidations.

H. *Ex situ* FTIR analysis of TPA-Py POP in charged and discharged state

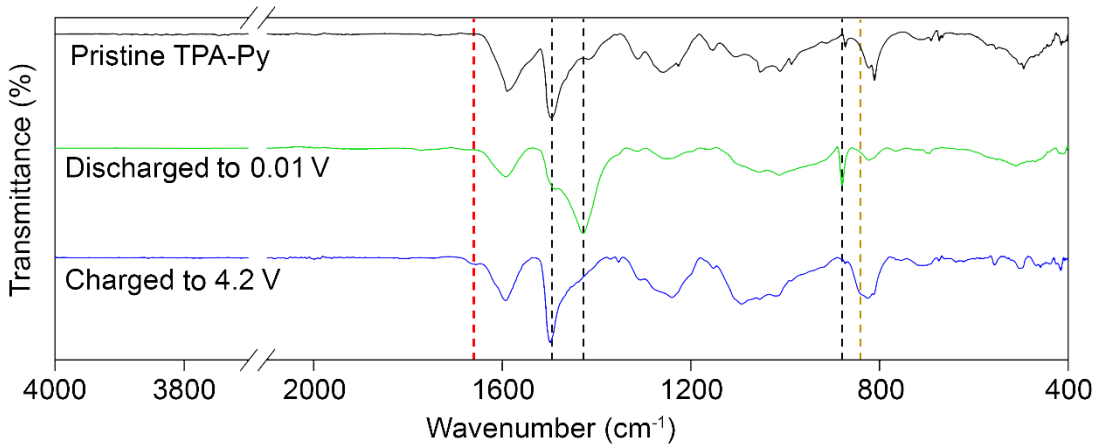

Fig. S16 Comparative *ex situ* FTIR spectra of TPA-Py polymer-based electrodes after charging/discharging at different potentials.

The mechanistic investigation of dual-ion storage by TPA-Py polymer was carried out using ex-situ FTIR analysis of the battery electrodes. The coin cells were fully discharged and charged at 0.01 and 4.2 V, respectively, before disassembling. The comparative FTIR spectra of the pristine electrode show the distinguishable peaks at 1495 cm^{-1} (-C=C-), and 815 cm^{-1} (C-H) of pyrene moieties in the pristine electrode (Fig. S15). The strong absorption peaks at 1495 cm^{-1} decreased substantially, and two new peaks appeared at 1427 and 879 cm^{-1} in the completely discharged electrode at 0.01V (Fig. S15). This change in FTIR spectra corroborates the n-doping process of pyrene moieties during Na^+ ion uptake.[S10] Whereas, when the TPA-Py containing half-cell charged to 4.2 V, two new peaks appeared at 1660 and 840 cm^{-1} from the stretching vibration of -C=N- from one of the quinoid-like structure of triphenylamine moieties and P-F stretching vibration, respectively (Fig. S15).[S11,12] The results suggest the dual-ion charge storage process by TPA-Py POP through the intercalation-insertion mechanism.

V. Computational analysis

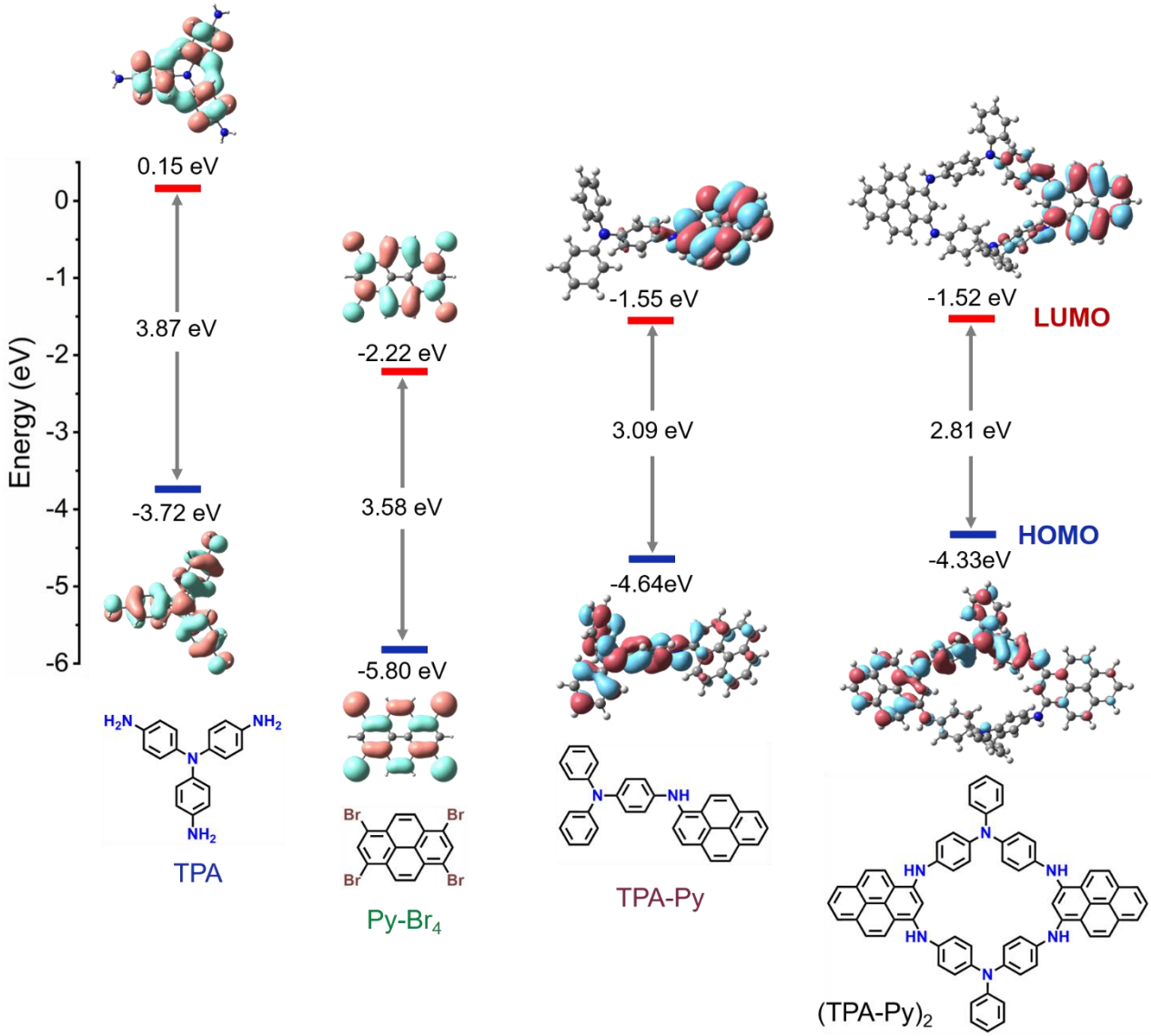

Fig. S17 Depiction of the optimized structures and the calculated HOMO-LUMO energy levels of the monomeric units (TPA and Py-Br_4) and polymeric repeating unit: 1:1 equivalent TPA and Py, 2:2 equivalent TPA and Py.

The electronic structures of the monomers and polymeric repeating units were computed using density functional theory calculation [B3LYP, 6-31G(d,p)] to get more insights into the electronic distributions. The smaller HOMO-LUMO energy gap of TPA-Py repeating units indicates higher electronic conduction compared to its monomers (Fig. S16). In order to identify the preferred location of Na^+ and PF_6^- ions in the polymer network, the molecular electrostatic potential (MESP) of the repeating unit (TPA-Py) was estimated. The MESP-mapped electron densities suggest the preferable localization of Na^+ ions near the pyrene unit, whereas PF_6^- ions reside closer to triphenylamine units (Fig. S17).

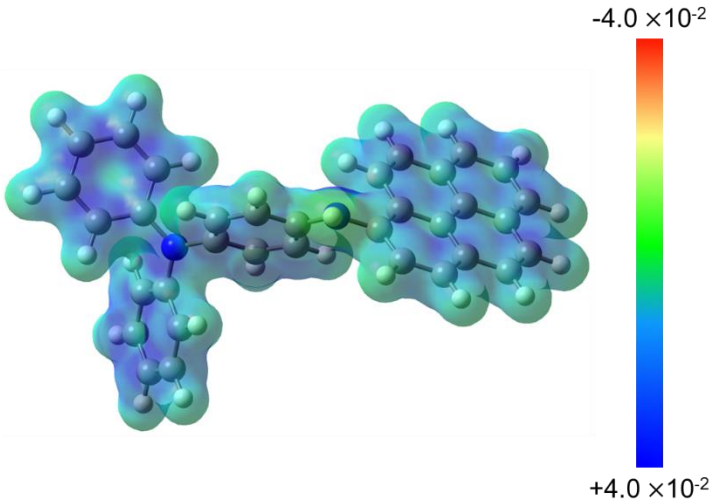

Fig. S18 Molecular electrostatic potential of repeating unit of TPA-Py porous organic polymer. Function: B3LYP; basis-set: 6-31G (d,p); isosurface value: 0.075.

VI. References

S1. S. Bandyopadhyay, C. Singh, P. Jash, M. W. Hussain, A. Paul and A. Patra, *Chem. Commun*., 2018, **54**, 6796-6799.

S2. Y. Z. Liao, H. G. Wang, M. F. Zhu and A. Thomas, *Adv. Mater*., 2018, **30**, 1705710.

S3. T. K. Dutta and A. Patra, *Chem. Asian J*., 2021, **16**, 158-164.

S4. M. Tang, S. Zhu, Z. Liu, C. Jiang, Y. Wu, H. Li, B. Wang, E. Wang, J. Ma and C. Wang, *Chem*, 2018, **4**, 2600-2614.

S5. A. Giri, S. Biswas, M. D. W. Hussain, T. K. Dutta and A. Patra, *ACS Appl. Mater. Interfaces*, 2022, **14**, 7369-7381.

S6. A. Laybourn, R. Dawson, R. Clowes, T. Hasell, A. I. Cooper, Y. Z. Khimyak and D. J. Adams, *Polym. Chem*., 2014, **5**, 6325-6333.

S7. L. Xiang, X. Ou, X. Wang, Z. Zhou, X. Li and Y. Tang, *Angew. Chem. Int. Ed.*, 2020, **59**, 17924-17930.

S8. K. V. Kravchyk, P. Bhauriyal, L. Piveteau, C. P. Guntlin, B. Pathak and M. V. Kovalenko, *Nat. Commun*., 2018, **9**, 4469.

S9. M. Jia, W. Zhang, X. Cai, X. Zhan, L. Hou, C. Yuan and Z. Guo, *J. Power Sources* **2022**, *543*, 231843.

S10. H. Li, J. Wu, H. Li, Y. Xu, J. Zheng, Q. Shi, H. Kang, S. Zhao, L. Zhang, R. Wang, S. Xin, T. Zhou and C. Zhang, *Chem. Eng. J*., 2022, **430**, 132704.

S11. H. Zhang, L. Zhong, J. Xie, F. Yang, X. Liu and X. Lu, *Adv. Mater*., 2021, **33**, 2101857.

S12. H. G. Wang, Q. Li, Q. Wu, Z. J. Si, X. L. Lv, X. T. Liang, H. L. Wang, L. Sun, W. D. Shi and S. Y. Song, *Adv. Energy Mater*., 2021, **11**, 2100381.